


Self-supporting smart air filters based on PZT/PVDF electrospun nanofiber composite membrane

Journal Article

Author(s):

He, Weidong; Guo, Yinghe; Zhao, Yi-Bo; [Jiang, Fuze](#) ; Schmitt, Jean; Yue, Yang; Liu, Jingxian; Cao, Junji; [Wang, Jing](#) 

Publication date:

2021-11

Permanent link:

<https://doi.org/10.3929/ethz-b-000485161>

Rights / license:

[Creative Commons Attribution-NonCommercial-NoDerivatives 4.0 International](#)

Originally published in:

Chemical Engineering Journal 423, <https://doi.org/10.1016/j.cej.2021.130247>



Self-supporting smart air filters based on PZT/PVDF electrospun nanofiber composite membrane

Weidong He^{a,b,c}, Yinghe Guo^{a,b,c}, Yi-Bo Zhao^{b,c}, Fuze Jiang^{b,c}, Jean Schmitt^{b,c}, Yang Yue^{b,c}, Jingxian Liu^{a,*}, Junji Cao^d, Jing Wang^{b,c,*}

^a Filter Test Center, Northeastern University, Shenyang, Liaoning 110819, China

^b Institute of Environmental Engineering, ETH Zürich, Zürich CH-8093, Switzerland

^c Lab of Advanced Analytical Technologies, Empa, Dübendorf CH-8600, Switzerland

^d Institute of Atmospheric Physics, Chinese Academy of Sciences, Beijing 100029, China

ARTICLE INFO

Keywords:

Self-supporting
Smart air filter
Sensors
Energy harvesting
Anti-bacteria

ABSTRACT

Smart air filters are beneficial to provide highly efficient particle removal, treat multiple contaminants simultaneously and conserve energy during air filtration processes. Herein, a type of self-supporting smart air filter (SSSAF) was fabricated by sandwiching the VOC-responsive PZT/PVDF electrospun membrane with two metal mesh electrodes. Besides the high filtration efficiency for sub-micron particles, the SSSAF showed good responses to pressure drop in the range of 0 to 500 Pa via the electroactivity of PZT/PVDF membrane. In addition, the SSSAF achieved VOC sensing function via the swelling properties of PZT/PVDF membrane in organic vapors, demonstrated by its signal to 50 to 200 ppm ethanol vapors. The SSSAF was employed to harvest wind energy, which was further applied to inhibit bacterial growth without the need of additional power input. Our SSSAF was designed to take advantage of the energy carried by the filtration air flow, which is necessary in any filtration system thus brings a stable and innate energy source. The results provide new insight into development of all-in-one smart air filters.

1. Introduction

Indoor air quality attracts public attention because people spend a major fraction of their time indoors [1]. Indoor contaminants include airborne particulates, volatile organic compounds (VOCs), and bio-aerosols, which could all induce respiratory diseases [2-5]. Moreover, bioaerosols and VOCs may cause infectious diseases, chronic toxicity, and cancer [6]. Polymer fibrous air filters are efficient for capturing airborne particulates and microorganisms, thereby have been widely used in hospitals, public and residential buildings for indoor air quality management [7-9].

High filtration efficiency is the basic requirement for an air filters. Polymer fibrous air filters capture particles through mechanical filtration mechanisms including interception, inertia impaction and Brownian diffusion, as well as electrostatic mechanisms such as image and columbic forces [10-12]. Traditional fibrous filters achieve high filtration efficiency by enhancing mechanical filtration effects, which come with high pressure drop and thus increase the operating cost [13]. For decades, electrostatic filters attracted attentions because they possessed

high filtration efficiency and low pressure drop. More recently, a smart self-powered triboelectric filter which generated triboelectric charges to enhance the filtration efficiency was developed [14-16]. Compared to traditional filters, the operating cost of electrostatic filters are lower because they rely more on electrostatic filtration mechanism to capture particles. However, the manufacturing cost of electrostatic filters is still high and replacement is required frequently. A growing research trend is to design and fabricate multifunctional air filters which are more energy efficient and allow multiple contaminants to be simultaneously removed [17]. So far, a combined filtration process with high particle filtration efficiency and VOCs removing function and a hierarchical porous filter capable of removing dusts, VOCs, and microorganisms have been introduced [17,18].

Improving the antibacterial property and VOC monitoring function is especially important for air filters used for indoor air quality control. Different from inert particulates, the microorganisms deposited on filters can generate secondary metabolites and increase the risk of respiratory diseases [19,20]. In order to reduce the risk of the harmful microbes deposited on filters, several types of antibacterial air filters

* Corresponding authors at: Institute of Environmental Engineering, ETH Zürich, Zürich, CH-8093, Switzerland (J. Wang).

E-mail addresses: liujingxian@mail.neu.edu.cn (J. Liu), jing.wang@ifu.baug.ethz.ch (J. Wang).

<https://doi.org/10.1016/j.cej.2021.130247>

Received 8 April 2021; Received in revised form 3 May 2021; Accepted 5 May 2021

Available online 11 May 2021

1385-8947/© 2021 The Author(s).

Published by Elsevier B.V. This is an open access article under the CC BY-NC-ND license

(<http://creativecommons.org/licenses/by-nc-nd/4.0/>).

were developed by adding chitosan, silver, ZnO, or TiO₂ nanoparticles [21-25]. However, these antibacterial air filters are not widely used because of the high cost of antibacterial additives. In terms of VOC degradation, thermal oxidation system and photocatalytic system are the most widely employed methods. Thermal oxidation requires high temperatures of 200 – 1200 °C, and the optimum temperature of photocatalytic reactions is between 20 and 80 °C [26-28]. Non-stop heating of the catalytic system to the reaction temperature leads to waste of energy and unnecessary operational costs. Monitoring VOC concentrations to determine the heating time improves the system sustainability. Currently, the detection of VOCs in filtration systems mainly depends on extra sensors, which gives rise to additional cost and energy consumption. Enabled by the recent advances in polymer science, several stimuli-responsive polymers, such as pH-responsive poly(4-vinylpyridine), [29] thermally sensitive poly(N-isopropylacrylamide) [30] and electroactive polyvinylidene fluoride (PVDF), [31] have been reported to be used as sensing materials. Fabricating smart air filters with stimuli-responsive polymers is expected to achieve multifunctional air filters. So far, a smart air filter with the combined properties of high filtration efficiency, embedded sensing function and antibacterial property has not been reported.

In the present study, a self-supporting smart air filter (SSSAF) based on the lead zirconate titanate/polyvinylidene fluoride (PZT/PVDF) electrospun nanofiber composite membrane was introduced. The PZT nanoparticles were added in polymer to improve the mechanical and electrical properties of the composite membranes. In general, PZT and PVDF are immiscible in the absence of specific interactions [32]. Rana *et al.*, conducted a systematic study in the area of polymer blends. The Flory-Huggins interaction parameter was used to explain the miscibility of the polymer blends, and a concentration range of miscibility for the polymers composition in the absence of specific interactions was observed [32-34]. The interaction parameter, which affects the flexibility of prepared polymer membrane, is an important parameter for the vibration-responsive PZT/PVDF membrane [35]. The studies of polymer blends provide a theoretical basis for preparing particle-polymer solutions and electrospun membranes, and help to understand the contributions of additives on the interface interaction. Thanks to the nanofiber structure, and the intrinsic piezoelectric property and swelling effect in organic vapor of the PZT/PVDF membrane, the SSSAF demonstrated excellent performance in terms of filtration efficiency, VOC and pressure drop sensing and bacterial inhibition. The results in this study provide new insights into development of multi-functional smart air filters.

2. Materials and methods

2.1. Materials

Poly(vinylidene fluoride) (PVDF, average Mw ~ 180000, CAS number 24937-79-9) and N, N-dimethylformamide (DMF, anhydrous, 99.8% CAS number 68-12-2) were purchased from Sigma-Aldrich. Acetone (≥99.5%, CAS number 67-64-1) was obtained from VWR. Lead zirconate titanate (99.9%) powder was purchased from QiJin New Material, China.

2.2. Fabrication and characterization of PZT/PVDF membrane

PVDF and PZT powder were dissolved in a mixture of DMF/acetone (1:1 wt%), forming a 14 wt% PZT/PVDF solution. PZT was mixed with PVDF in weight ratios of 0%, 0.5%, 1% and 2%. A multi-jet electrospinning system (NaBond Technologies Co., Ltd.), consisting of three spinnerets and a rotating drum collector, was used for the fabrication of nanofiber membranes. A tip-to-collector distance of 10 cm, a solution flow rate of 1 ml/h and a voltage of 20 kV were applied. All PZT/PVDF membranes were dried in a vacuum oven at 70 °C for 24 h to fully evaporate the solvent. The morphology of the electrospun PZT/PVDF membrane was characterized by scanning electron microscopy (SEM,

Quanta FEG 650). Image J software was utilized for analyzing the average diameter of nanofibers. The crystalline phase of the PZT/PVDF membrane was identified by X-ray diffraction (XRD, Bruker D8).

2.3. Fabrication of the self-supporting smart air filter (SSSAF)

Organic solvents/vapors induced resistance changes of swelling polymer is the basic principle of VOC sensing for the SSSAF, thus a conductive area serving as the electrode was fabricated on the PZT/PVDF membrane. A series of square gold particle layers with different areas (1, 2, 3, 4, 5 mm²) and thicknesses (10, 20, 30, 40, 50 nm) were produced in the middle of the PZT/PVDF membranes by magnetron sputtering (Leica, EM ACE 600). By comparing the resistance and response time to ethanol vapor, we selected an optimized gold particle layer with the 1 mm² area and 40 nm thickness. As the VOC sensing area, the two edges of this square were separately connected to a multimeter with wires to collect the response signal (Fig. 1a).

Two metal mesh electrodes were adopted to produce equal but opposite charges via the electrostatic induction of the piezo generated potential at the interface, and connected with the signal collection instruments and energy storage circuit. The PZT/PVDF membrane was sandwiched between the two metal mesh electrodes which were connected with wires to other devices separately (Fig. 1a), then the edge of the sandwiched PZT/PVDF membrane was sealed with a rubber ring. The two metal mesh electrodes had the mesh opening of 2 × 2 mm and negligible pressure drop. In addition, a set of windmill blades driven by the air flow was set in front of the SSSAF to strike the filter to generate vibration.

2.4. Piezoelectric characterization of SSSAFs

The piezoelectric voltage of the SSSAFs equipped with different PZT/PVDF membranes were evaluated by a test platform as shown in Figure S1a. The SSSAF was clamped in a filter test chamber; a set of windmill blades driven by the air flow was set in front of the SSSAF to strike the filter to generate vibration. The piezoelectric signal generated by the vibration of SSSAF was recorded by a digital multimeter (Keithley, DMM 7510).

2.5. Particle filtration test for the SSSAFs

The filtration efficiency of the SSSAF was measured by a test platform (Figure S1a). Polydisperse NaCl aerosol was generated by an atomizer (TSI 3079A) and dried by a diffusion dryer. A differential mobility analyzer (DMA, TSI 3081) was used to select the particles with the target diameters. In this work, the particles with the mobility diameters of 30, 50, 80, 100, 200, 300, 400, and 500 nm were selected. Two condensation particle counters (CPC, TSI 3775) were employed to measure the particle concentrations up- and down-stream, aiming to calculate the particle filtration efficiency of the filter. To understand the effects of the windmill blades on the filtration efficiency, the particle filtration test of the SSSAF was performed under both static (without the windmill blades striking the filter) and vibration conditions (with the windmill blades striking the filter). The face velocity of test was 5.3 cm/s.

2.6. Evaluation of the VOC sensing functions

The resistive response of the VOC sensor under controlled environment was characterized by using the setup shown in Figure S1b. A water bubbler was used to control the relative humidity within 40%-60%, and the temperature was kept at 25 °C via a heated mantle. First, the SSSAF was installed in the gas test chamber sealed with Teflon tape, while the wires of the VOC sensor were connected to the digital multimeter. Second, ethanol gases at different concentrations were prepared by diluting the pure ethanol gas with nitrogen, then the ethanol gas was fed

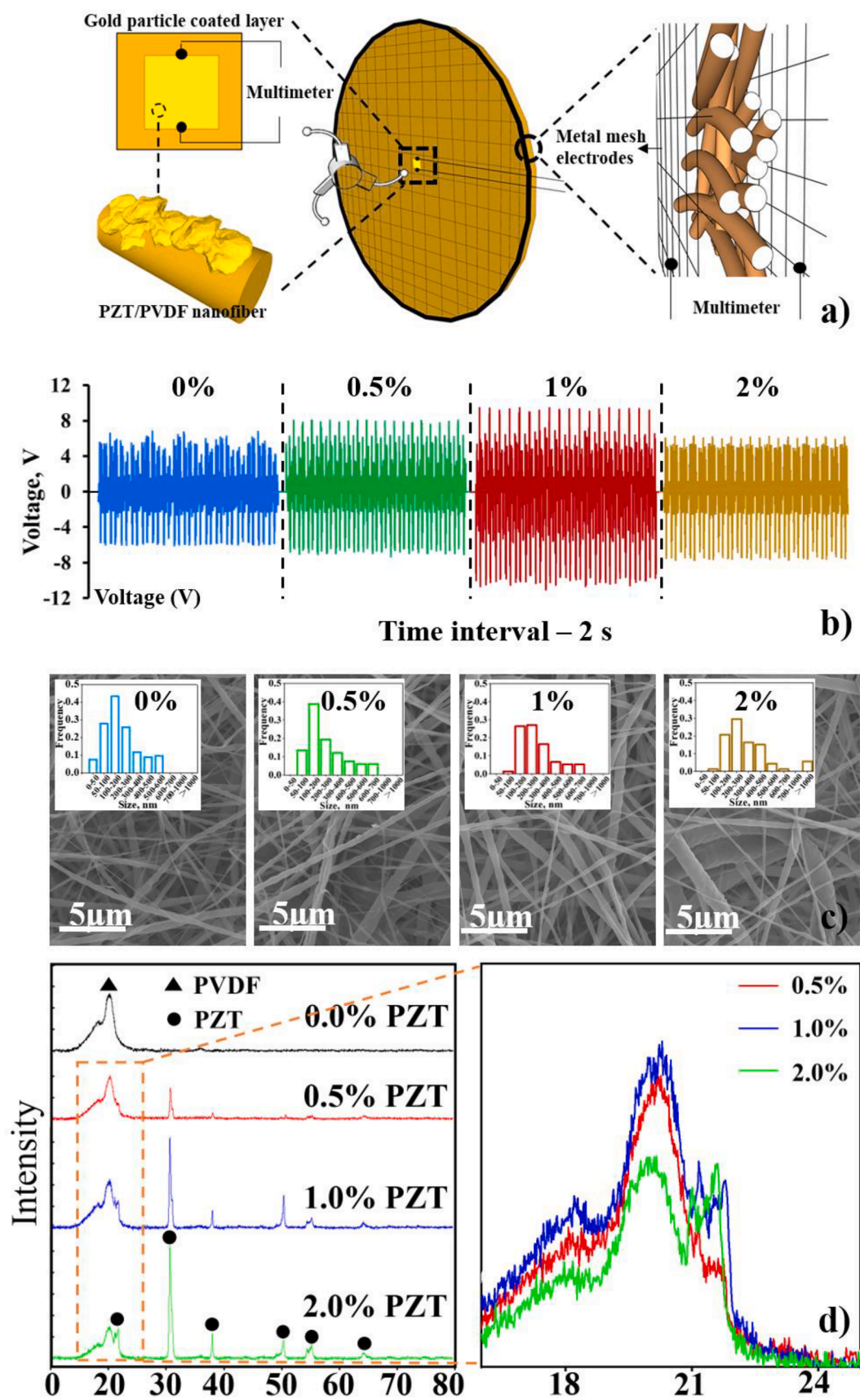


Fig. 1. a) The schematic diagram of the SSSAF; b) The output voltage of the SSSAF equipped with different PZT/PVDF membranes; c) SEM images of PZT/PVDF membranes with different PZT concentrations, and the diameter distributions of PZT/PVDF fibers. d) XRD patterns of PZT/PVDF membranes with different PZT concentrations.

into the gas test chamber at a constant flow rate of 10 ml/min. The sensor measurement consisted of exposure to the ethanol gas until the response signal stabilized and a subsequent purging with dry nitrogen to reset the baseline. The signal generated by dry nitrogen with equivalent flow rate of the ethanol gas was defined as the baseline for the sensor. Herein, the sensor responses were presented as the resistance difference between the response and baseline ($\Delta R = R_{\text{response}} - R_{\text{baseline}}$). The test concentrations of ethanol gas were in the range of 50 to 200 ppm.

2.7. Evaluation of the pressure drop sensing functions

On the basis of the filtration test platform shown in Figure S1a, with the steps of particle selection by DMA and particle concentration measurement by CPC skipped, the polydisperse NaCl aerosol were directly loaded on the SSSAF after being dried and neutralized. The pressure drop of the SSSAF was measured by a pressure transducer (OMEGA PX409-10WDWUUSBH) during particles loading, and the piezoelectric voltage signals corresponding to the growth in pressure drop of 0, 100, 200, 300, 400 and 500 Pa were recorded via the digital multimeter.

2.8. Energy harvesting and bacteria inhibition

The electroactive materials were usually used to harvest energy from ambient environments (e.g. human activities, ocean waves, mechanical vibration, wind) via piezoelectric effects. Herein, the SSSAF equipped with piezoelectric PZT/PVDF membrane was used to harvest wind energy by coupling with an energy storage circuit consisting of two diodes and two capacitors (Figure S1c). The alternating current (AC) voltage generated by the SSSAF was first half-wave rectified and then stored in two capacitors which could be used in series. Compared with the full wave rectifier, less diodes of our circuit made it more compact and led to less power dissipation. During the wind energy harvesting, the windmill blades were driven by air flow of 5.3 cm/s which was the same flow rate as that in the particle filtration test.

The harvested energy was used to inhibit the growth of bacteria on the SSSAF in the form of electrical discharge. In the present work, the bacterial cells on filters before and after electric discharge treatment had similar morphologies (Figure S2). The status of bacteria before and after inactivation process cannot be distinguished via SEM images, therefore, the colony counting method was used to evaluate the antibacterial effect. The used model bacteria were *Bacillus Subtilis* (*B. Subtilis*) and *Escherichia coli* (*E. coli*). The bacteria were cultured in 50 ml liquid Luria Bertani (LB) broth (10 g/L tryptone, 5 g/L yeast extract and 5 g/L sodium chloride) in an incubator at 37 °C and 50% RH for 24 h. Next, the bacteria were separated from the LB liquid broth by centrifuge and prepared as a bacteria-water suspension at the concentration of 1.0×10^7 cell/ml. 200 μ L bacteria-water suspension was pipetted into a vial, then dispersed by an air jet nebulizer and sprayed on the SSSAF by compressed air with 2 bar pressure. The spraying system and bacteria distribution were shown in Figure S3 and Figure S2, respectively. An electrical discharge at 4 V voltage was applied on the filter surface loaded with bacteria at a frequency of 14 times per hour. The electrical discharge was performed by the SSSAF energy harvester. After electrical discharge treatment, the PZT/PVDF membrane inside the SSSAF was taken out and eluted with 10 ml water, then 100 μ L eluent was spread on the prepared LB agar plates (15 g/L agar, 10 g/L tryptone, 5 g/L yeast extract and 5 g/L sodium chloride) and cultured in the incubator at 37 °C and 50% RH for 24 h. The number of bacteria colonies were counted and compared with the control sample. The SSSAF, water, and broth were sterilized before use.

3. Results and discussion

3.1. Piezoelectric property of the SSSAF

The peak output voltage of the SSSAF equipped with the PZT/PVDF

membrane was influenced by the PZT concentration (Fig. 1b). First, the dielectric constant of the PZT/PVDF membrane was enhanced by the addition of PZT powder, leading to increase of the peak output voltage [36]. Second, the increasing PZT concentration led to the fibers with bigger diameters (Fig. 1c). Due to the higher mass, the bigger fibers generated less vibration in response to the external mechanical stimulation, and finally resulted in lower output voltage when the PZT concentration was too high. The positive effect of PZT on the piezoelectric property was predominant when the PZT concentration was less than 1%, whereas the negative effect of PZT was more obvious when the PZT concentration increased to 2% (Fig. 1b and Fig. 1c).

The high fraction of the β crystalline phase in PVDF may be another reason for 1% being the optimal PZT concentration in the PZT/PVDF membrane. With the addition of the PZT powder, the intensity of the PZT characteristic peaks in the XRD pattern increased, while the intensity of the PVDF characteristic peak became lower compared to pure PVDF (Fig. 1d). Among the membranes loaded with different PZT concentrations, the PZT/PVDF membrane with a PZT concentration of 1% demonstrated the maximum intensity of the characteristic peak at $2\theta = \sim 20^\circ$, which indicated high fraction of the β crystalline phase of PVDF molecules (Fig. 1d). PZT served as a source of the electric field during polarization and promoted the transformation of other polymer phases into the β crystalline phase [37]. On the other hand, finer electrospun PVDF nanofibers showed higher fraction of the β crystalline phase [38]. Due to the above two competing effects, the highest fraction of the β crystalline phase in the PZT/PVDF fibers occurred at a finite PZT concentration which was found to be around 1% in the present study.

The piezoelectric performance of the SSSAF was affected by the area and thickness of the PZT/PVDF membrane. For the PZT/PVDF membranes with the same thickness of 110 μ m, the peak output voltage increased from ~ 3 to ~ 12 V when the membrane area increased from 11 to 100 cm^2 (Figure S4a). With the PZT/PVDF membrane area of 66 cm^2 , the peak output voltages with thicknesses of 62.5, 75 and 110 μ m were ~ 4 , ~ 6 and ~ 10 V, respectively (Figure S4b). The method to measure the membrane thickness is illustrated in Figure S5. In addition, several materials commonly used as filtration media were selected as reference samples to prove the voltage signal was generated due to the specific properties of the PZT/PVDF membrane. The results showed that the piezoelectric voltage signals of paper filter, PTFE membrane and nylon membrane were negligible compared with the PZT/PVDF membrane (Figure S4c).

3.2. Filtration efficiency of the SSSAF

As shown in Fig. 2, the SSSAF equipped with the thicker PZT/PVDF membrane possessed higher filtration efficiency and smaller most penetrating particle size (MPPS). Similar influences of the filter thickness on filtration efficiency and MPPS were observed in previous works [39,40]. Huang et al., attributed the enhancement of filtration efficiency to the increased particles deposition sites in the thicker filter [40]. Compared with the thinner membrane, the thicker PZT/PVDF provided additional filtration medium which could be considered as an extra electret filter. It is well known that the electret filters can have small MPPS well below 100 nm [41]. Overall, the filtration efficiencies of the SSSAFs were higher than 97% for particles below 100 nm, and > 99% for particles over 200 nm. According to the filtration test results, the windmill blades had no statistically significant effects on the filtration efficiency of the SSSAF. The PZT/PVDF membrane with a thickness of 110 μ m presented the highest filtration efficiency. In the following tests, the SSSAF was equipped with PZT/PVDF membrane with a PZT concentration of 1%, an area of 100 cm^2 and a thickness of 110 μ m.

3.3. Performance of the SSSAF on pressure drop sensing

The pressure drop and the piezoelectric signal of the SSSAF, both affected by the loaded particles, was correlated. For example, the output

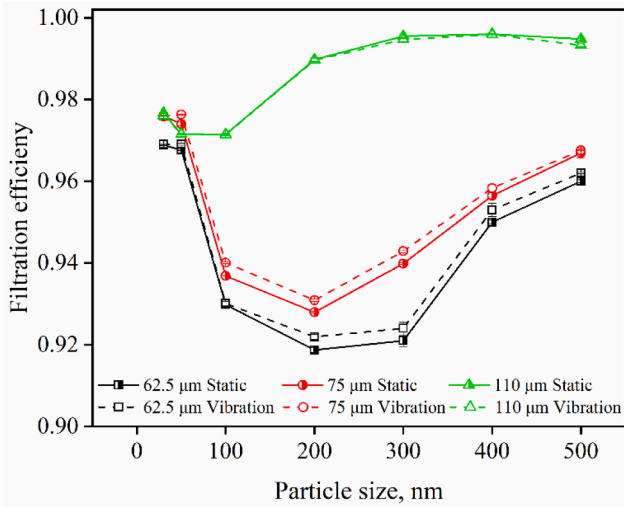


Fig. 2. Particle filtration efficiencies of the SSSAFs equipped with different PZT/PVDF membranes with and without the striking blades. The test velocity was 5.3 cm/s and the pressure drops corresponding to 62.5, 75 and 110 μm PZT/PVDF membranes were 130, 195 and 320 Pa, respectively.

top peak voltage decreased from ~ 5 to ~ 1 V with the pressure drop changing (ΔP) of the SSSAF increased from 0 to 500 Pa (Fig. 3a and Figure S6). Each pressure drop could be correlated to a specific top peak voltage signal, and the peak voltages generated by SSSAF at different pressure drops had statistically significant difference. Moreover, the pressure drop sensing of three SSSAFs were consistent, the relative differences of the peak voltages generated by SSSAF 2 and SSSAF 3 were less than 5% compared to SSSAF 1 (Table S1). A fitting equation between the output voltages and pressure drops was derived from the experimental results of three SSSAFs equipped with the same type of PZT/PVDF membrane. As shown in Fig. 3b, within the ΔP range of 0–500 Pa, ΔP and the output peak voltage were linearly related.

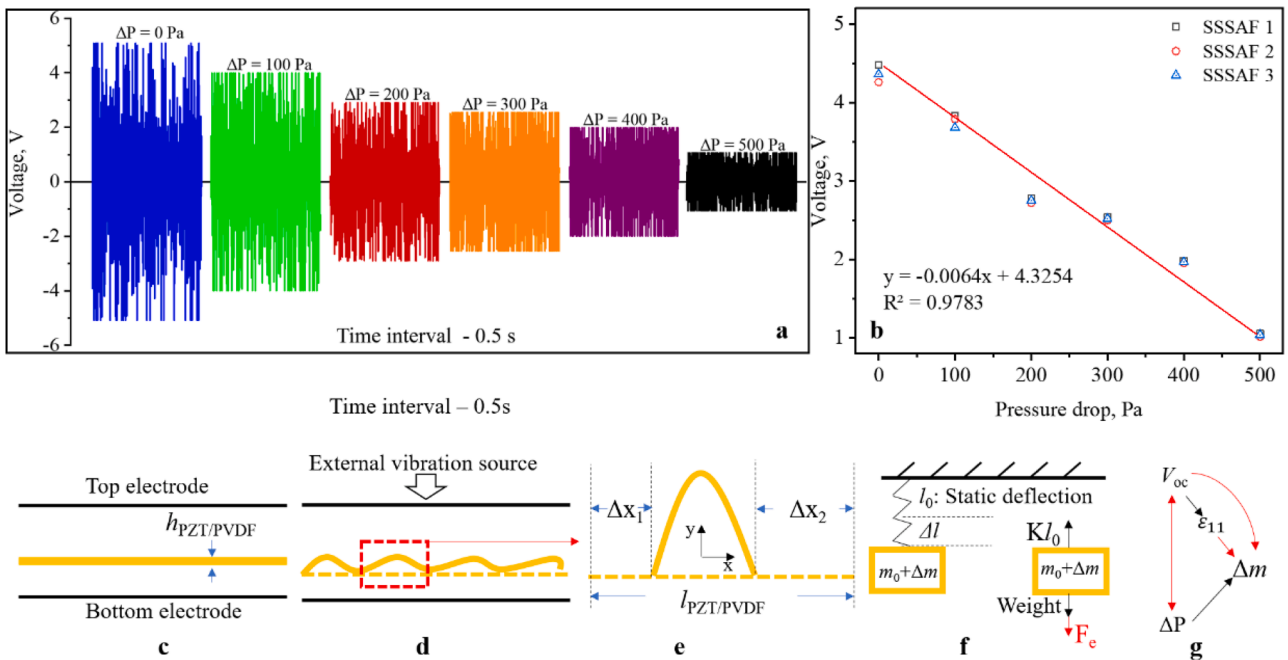


Fig. 3. a) The decreasing output voltages of a SSSAF (SSSAF 1) with the pressure drop increasing; b) The fitting equation between the output voltages and pressure drops based on the experimental results of three SSSAFs with the same PZT/PVDF membrane; c) Scheme of the PZT/PVDF based SSSAF; d) Schematic view of the vibration of PZT/PVDF under external force; e) Model of a wave unit in one vibration cycle; f) An undamped spring mass system equivalent to one wave unit of PZT/PVDF membrane vibration; g) The derived logic between V_{oc} and ΔP .

As mentioned above, the pressure drop sensing of SSSAF was based on monitoring of open-circuit voltage [42]. The open-circuit voltage of the piezoelectric membrane is given by [42],

$$V_{oc} = I_{sc} R_i \quad (1)$$

where R_i is the inner resistance of the piezoelectric material; I_{sc} is derived from,

$$I_{sc} = 2\pi d_{31} \gamma E A_E f \varepsilon_{11} \quad (2)$$

where d_{31} is the piezoelectric coefficient, E is the Young's modulus of the material, γ is a geometry effect parameter, A_E is the effective working area of the piezoelectric membrane, f is the loading frequency, and ε_{11} is the normal strain of the membrane. R_i , d_{31} , and E only depend on the material itself, γ depends on the geometry of electrodes. In the present work, the air flow with the constant face velocity transferred steady momentum to the rotating blades, leading to a stable rotating speed, therefore striking the SSSAF with a constant loading frequency (f). $2\pi d_{31} \gamma E f R$ was considered as a constant λ , then Eq. (1) can be rewritten as

$$V_{oc} = \lambda A_E \varepsilon_{11} \quad (3)$$

As shown in Fig. 3c–3e, assuming that in each vibration cycle the PZT/PVDF membrane vibrates in the shape of a periodic wave, and each wave unit can be approximated by a sine function. The normal strain ε_{11} can be determined by the expression [42],

$$\varepsilon_{11} = \frac{2\pi h_{PZT/PVDF}}{l_{PZT/PVDF}^{3/2}} \cos\left(\frac{2\pi x}{l_{PZT/PVDF}}\right) \sqrt{\Delta x} \quad (4)$$

where $h_{PZT/PVDF}$ and $l_{PZT/PVDF}$ are the thickness and length of PZT/PVDF membrane, respectively; Δx is the deformation of PZT/PVDF membrane (see Fig. 3),

$$\Delta x = \Delta x_1 + \Delta x_2 \quad (5)$$

Δx is related to the mass of PZT/PVDF membrane and the loaded dust, however, it is difficult to identify the effects of mass on Δx in such a complex forced vibration of PZT/PVDF membrane induced by external force. In order to analyze the vibration process, we treated one wave unit in one vibration cycle (Fig. 3e) as a forced vibration of an undamped spring-mass system which is shown in Fig. 3f. Therefore, the equation that defines the motion of the mass can be expressed as [43]:

$$\frac{(m_0 + \Delta m)}{g_c} \frac{\Delta l}{\Delta t^2} + K(l_0 + \Delta l) = F_0 \sin(ft) \quad (6)$$

Δl is the deflection of the spring, which is equal to Δx . When external force F_0 is applied,

$$\Delta l = \frac{g_c \Delta t^2 [F_0 \sin(ft) - Kl_0]}{Kg_c \Delta t^2 + (m_0 + \Delta m)} \quad (7)$$

where g_c is a constant which has the same numerical value as gravitational acceleration, F_0 is the external force, f is the forced frequency (the loading frequency), K is the spring constant, l_0 is the static deflection of spring, m_0 and Δm are the initial mass and increased mass, respectively.

Herein, the mass in the undamped spring-mass system is that of the PZT/PVDF membrane. As the particles were loaded on the PZT/PVDF membrane, the effective mass of the membrane increased. According to Eqs. (3)(4)(7), the increased PZT/PVDF membrane mass reduced the deformation of PZT/PVDF membrane Δx , and further decreased the normal strain ε_{11} , and finally led to the decreasing of V_{oc} . The pressure drop increases with the loaded particle mass [44]. A logic shown in Fig. 3g was established. In addition, the effective work area (A_E) was changed during the particles loading. The A_E change can be explained that the loaded particles shielded the fibers, thus reducing the contact area between the piezoelectric PZT/PVDF membrane and the metal mesh electrodes.

In summary, the loaded particles on PZT/PVDF membrane decreased the output voltage and increased the pressure drop of SSSAF, therefore the voltage of SSSAF declined with the growing pressure drop (ΔP). The experimental results confirmed this analysis qualitatively. Due to the complex nature of the analysis, we were not able to derive a closed-form equation for the relationship between V and ΔP . For simplicity, a linear fitting was performed between V and ΔP as shown in Fig. 3b. In practical applications, calibration experiments can be performed to provide the dependence of V and ΔP , then the SSSAF can provide information for when to clean or replace the filter without the need of a differential pressure meter.

3.4. Performance of the SSSAF on VOC sensing

3.4.1. The selection of the thickness and area of the gold particle layer

For the thickness selection, we produced a series of gold particle layers on PZT/PVDF membrane with an area of 1 mm² and different thicknesses of 10, 20, 30, 40, 50 nm. For each thickness, the resistance of five gold particle layers was tested, the results were shown in Table 1. The 10 and 20 nm gold particle layers were non-conductive because the gold particles deposited on the fibers could not form a continuous structure. When the thickness increased to 30 nm, most of the gold particle layers were conductive. However, there was still a non-conductive 30 nm gold particle layer among the five tested samples, which might have been induced by the defects on the membrane surface. The resistance of gold particle layers kept stable when the thicknesses were 40 and 50 nm. As a result, at least a 40 nm gold particle layer was needed to produce a stable conductive section serving for VOC sensing. In addition, the response time to 50 ppm ethanol vapor was tested to compare the gold particle layers with thicknesses of 40 and 50 nm. As shown in Fig. 4a, the 40 nm gold particle layer presented faster response time and stronger response intensity compared to 50 nm gold particle

Table 1

The resistances of gold particle layers with an area of 1 mm² and different thicknesses.

Thickness (nm)	Resistance (Ω)					Average	Standard Deviation
	S1	S2	S3	S4	S5		
10	∞	∞	∞	∞	∞	–	–
20	∞	∞	∞	∞	∞	–	–
30	57	25.9	40.7	∞	80	–	–
40	2.8	3.2	2.6	2.7	3.1	2.88	0.26
50	2.1	2	1.8	1.6	2.3	1.96	0.27

layer. It was more difficult for the fiber swelling to produce cracks in the thicker gold particle layer, and finally resulted in the thicker gold particle layer demonstrated longer response time and weaker response intensity in ethanol vapor. Therefore, the gold particle layers with a thickness of 40 nm was selected in the present study.

For the area selection, we produced a series of gold particle layers on PZT/PVDF membrane with a thickness of 40 nm and different areas of 1, 2, 3, 4, 5 mm². For each area, the resistance of five gold particle layers was tested, and the results were shown in Table S2. As the area increased, the standard deviation among the five tested gold particle layers with the same area and thickness increased. In all the tested gold particle layers with an area from 1 to 5 mm², the smallest resistance variation was observed in 1 mm² gold particle layers (with a standard deviation of 0.26 Ω). The small resistance difference is beneficial to control the initial resistance of different gold particle layers with the same area and thickness to be consistent. Therefore, the 1 mm² gold particle layer was selected in the present study.

3.4.2. The response of SSSAF to ethanol vapor with different concentration

As shown in Fig. 4b, the complete response processes of the SSSAFs to ethanol vapor with different concentrations were provided. As the ethanol vapors were introduced into the test chamber, the ΔR of the VOC sensing section on SSSAF increased. During the response process, the measured resistance was observed to fluctuate and grow at the initial stage. The response times (time to reach 90% of the saturated ΔR value) of the SSSAF for 50, 100, 150, and 200 ppm ethanol vapors were 49 ± 10 , 130 ± 12 , 81 ± 7 , 79 ± 8 s, respectively. The saturated ΔR value increased from 21.7 ± 0.8 to 155.9 ± 18.3 Ω with the ethanol concentration increasing from 50 to 200 ppm, and it demonstrated a linear response toward the ethanol concentration. A specific response vs. VOC-concentration equation was derived from the calibration experiment of three SSSAFs (Fig. 4c). The responses of three tested SSSAFs to ethanol vapors with different concentrations were shown in Table 2. The measured biggest standard deviation between three tested SSSAFs at different ethanol concentrations was 18.3 Ω .

In a previous work about a polymer-based resistive VOC sensor, the response time of ~ 30 s and recovery time of ~ 200 s were achieved when chloroform was used to challenge the sensor [45]. Here, we observed the response time of the sensor was ~ 40 s for ethanol vapor and the sensor fully recovered as the ΔR value returned to the baseline within ~ 550 s after flushing the test chamber with dry nitrogen (Fig. 4d).

The absorption of ethanol vapor swelled the PZT/PVDF fibers and further produced cracks in the VOC sensing area (the gold particle layer) on the membrane. The cracks led to discontinuities in the gold particle layer, which caused increase of the resistance. The response to the ethanol concentration depended on the swelling degree of the PZT/PVDF membrane and the affinity of the PZT/PVDF fibers towards ethanol. The cracks healed after ethanol evaporation, thereby restoring the conductivity of the sensing element. In our previous work, swelling of various degrees was observed when polymer fibers were exposed to different organic compounds, which demonstrated the possibility to achieve the selectivity of the polymer based sensors for various VOCs [46]. In order to analyze the VOC sensing process, the resistance of a single fiber coated with the gold particle layer was discussed. The analysis was based on the assumptions that the gold particle layer is transformed into an isosceles triangle with an apex angle of θ by the crack and that only one crack is formed along x direction or y direction at a time (Fig. 5a). According to Ohm's law, the resistance of the gold particle layer (R) is given by:

$R = \rho \frac{l}{A}$ (8) where ρ , l , and A are, respectively, the resistivity, the length, and the cross sectional area of the gold particle layer. Therefore, the resistance of the gold particle layer with a crack along x direction (R_x) and y direction (R_y) are as follows,

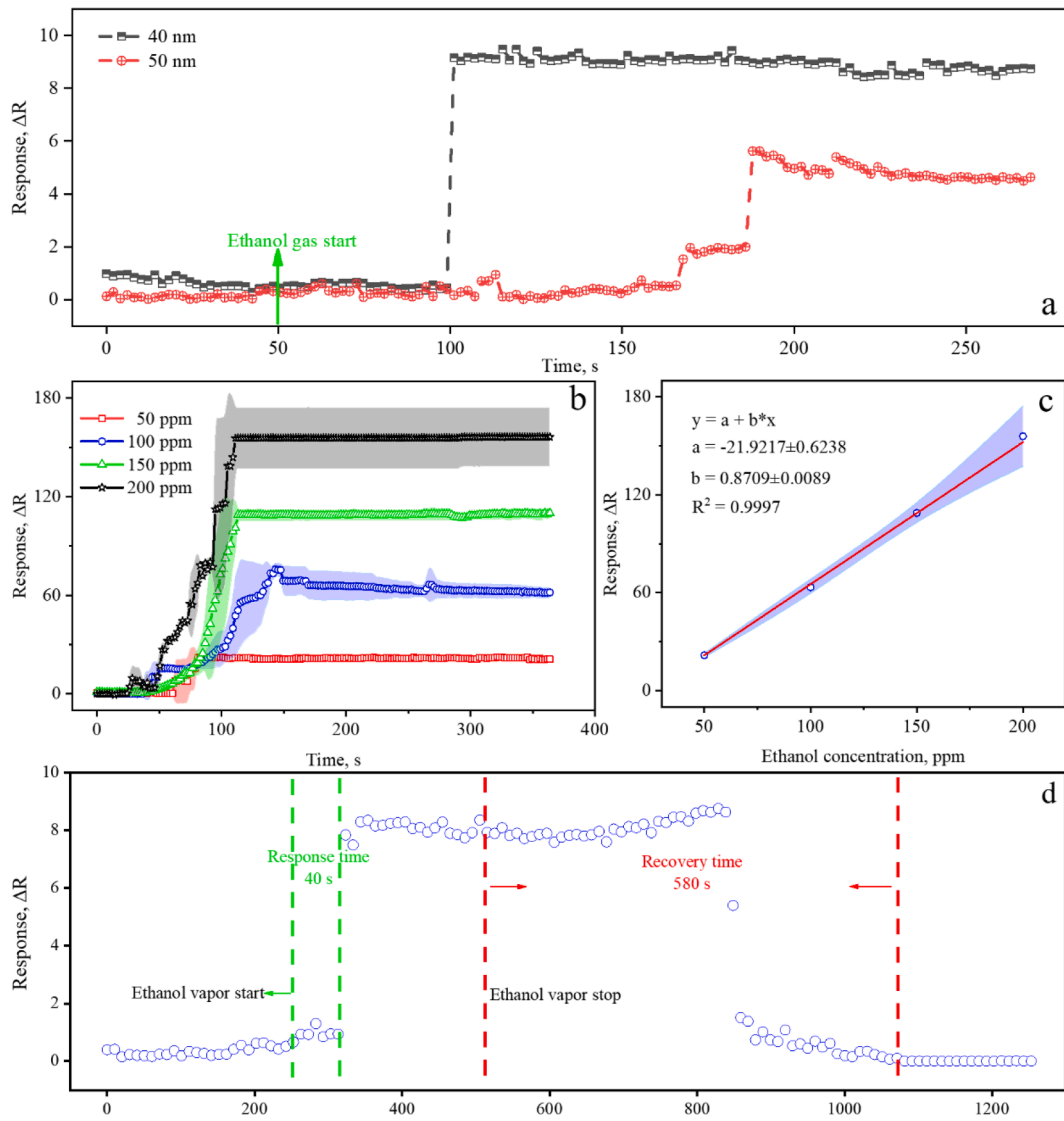


Fig. 4. a) The responses of SSSAFs with 40 and 50 nm gold particle layers to 50 ppm ethanol vapor; b) The response of SSSAFs with 40 nm gold particle layer to different ethanol vapor concentrations; c) The sensor response vs. VOC-concentration curve leading to a specific fitting equation of the SSSAF. d) The response time and recovery time of a SSSAF to 50 ppm ethanol concentration.

Table 2

The responses of three tested SSSAFs to ethanol vapors with different concentrations.

Ethanol concentration ppm	Response (ΔR), Ω SSSAF1	Response (ΔR), Ω SSSAF2	Response (ΔR), Ω SSSAF3	Average value, Ω	Standard deviation, Ω
50	22.6	21.2	21.3	21.7	0.8
100	60.7	63.8	70.6	65.0	5.0
150	105.6	109.7	111.5	108.9	3.0
200	140.9	150.4	176.3	155.9	18.3

$$\begin{cases} R_x = \rho \frac{l_0}{w_0(h_0 - h_{crack-y})} \\ R_y = \rho \frac{w_0}{l_0(h_0 - h_{crack-x})} \end{cases} \quad (9) \text{ where } l_0, w_0 \text{ and } h_0 \text{ are the original}$$

length, width and height of the gold particle layer, respectively; $h_{crack-y}$ and $h_{crack-x}$ are, respectively, the height of crack along y direction and x direction.

For the gold particle layer with a crack along y direction (case 1 shown in Fig. 5b), the following equations can be obtained,

$$\Delta l = (r_0 + \Delta r + h_0) \tan \alpha - l_0 \quad (10)$$

$$h_{crack-y} = \frac{1}{2} \frac{\Delta l}{\tan(\theta/2)} \quad (11)$$

By substituting Eq. (10) into Eq. (11), we obtain

$$h_{crack-y} = \frac{(r_0 + \Delta r + h_0) \tan \alpha - l_0}{2 \tan(\theta/2)} \quad (12)$$

For the gold particle layer with a crack along x direction (case 2 shown in Fig. 5b), the following equations can be obtained,

$$\Delta w = \frac{\pi(r_0 + \Delta r + h_0)}{2} - w_0 \quad (13)$$

$$h_{crack-x} = \frac{1}{2} \frac{\Delta w}{\tan(\theta/2)} \quad (14)$$

Substituting Eq. (13) into Eq. (14), then

$$h_{crack-x} = \frac{\pi(r_0 + \Delta r + h_0) - 2w_0}{4 \tan(\theta/2)} \quad (15)$$

From equations (9) (12) (15), as the radius of swelled fiber increasing, the height of crack increased, therefore the effective cross sectional area decreased, and finally caused that the resistance of the gold particle layer increased. The radius change (Δr) depends on the degree of fiber swelling when the fiber was exposed to organic solvent. In a previous work, the fibers with original diameters in the range of 10–20 μm were immersed in organic liquid and the fiber diameters after swelling were observed/calculated by microscope and capillary rise methods [47]. In the present work, the fiber diameters were below 1 μm

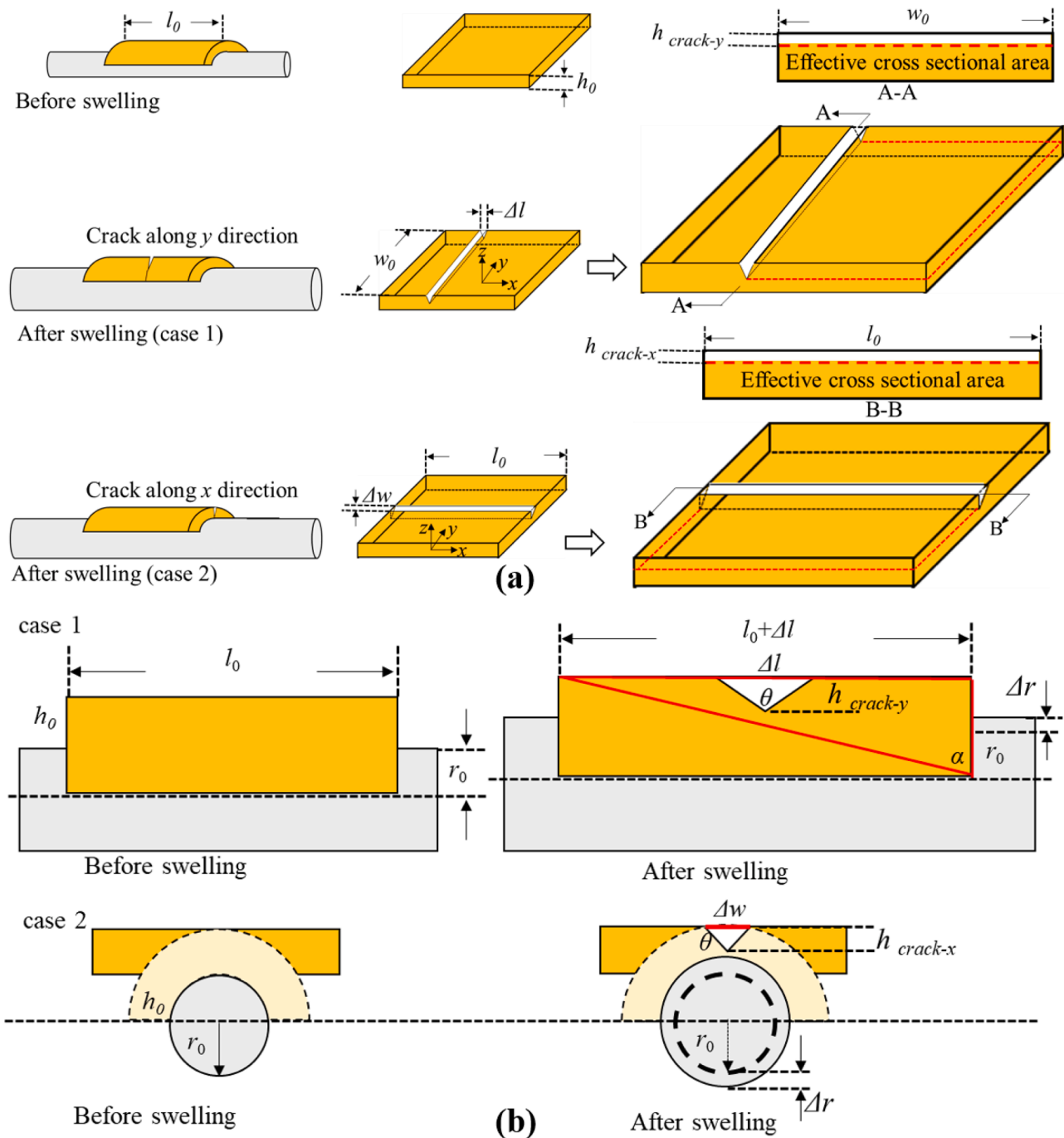


Fig. 5. a) Schematic view of the swelling of a single fiber along different directions; b) Model of the fiber radius change after swelling.

and the highest used ethanol concentration was 200 ppm, consequently we were not able to quantify the changes in fiber diameter by microscopy and the proposed model could only qualitatively explain the experimental results.

3.5. Energy harvesting and bacteria inhibition

Three AC voltage signals generated by the SSSAF (Figure S7), with the peak voltage values (V_{max}) of 6, 7, and 8 V, were used for capacitor charging. The capacitors were charged at the highest speed at the beginning, then the charging speed slowed down, eventually reaching the saturation voltages of ~ 2.8 , 3.2 and 4.0 V, respectively (Fig. 6a). The saturation voltages (V_S) of the capacitors were $\sim 50\%$ of the V_{max} of pulsed AC signal generated by the SSSAF based nanogenerator. V_S

depends on the energy transfer efficiency of the energy storage unit. It is well known that the rectifier used in the energy storage unit consists of diodes with a forward voltage (V_F). The diodes were at "off" state when the voltage supplied by the nanogenerator was lower than V_F , which induced the loss of energy and thus V_S was smaller than V_{max} [48]. Zi et al., proposed a plot of the built-up voltage V against the transferred charges Q to analyze the charging process of a triboelectric nanogenerator for batteries/capacitors, and provided an equation to calculate the V_S [49]:

$$V_S = \frac{V_{max} V'_{max}}{V_{max} + V'_{max}} \quad (16)$$

where V_{max} is the maximum open-circuit voltage at $Q = 0$, and V'_{max} is the maximum achievable absolute voltage when Q is equal to the maximum short-circuit transferred charge. In the present study, the

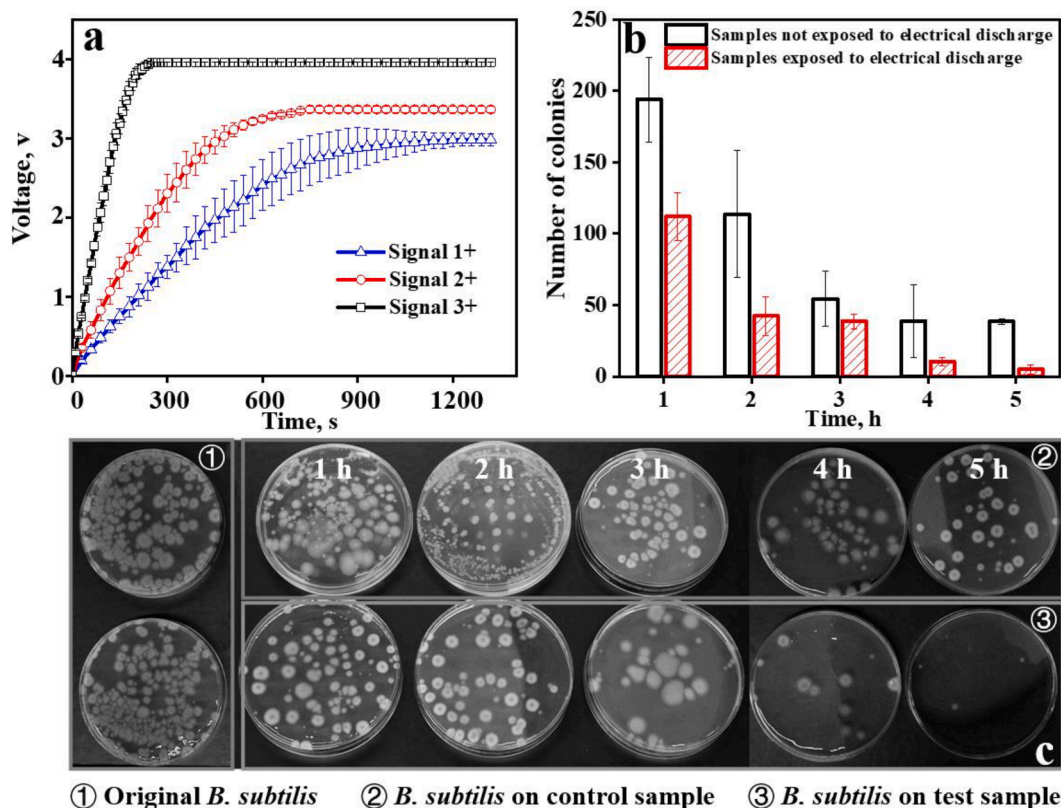


Fig. 6. Test results for the special functions of the SSSAF. a) Charging curves of the 10 μF capacitor by the different levels of power generated by the SSSAF based nanogenerator (signal + represents the positive half cycle of the AC signal). b) Bacteria inhibiting effect of the electrical discharge generated from the harvested energy. c) Petri dishes for counting of bacteria-formed colonies.

SSSAF based nanogenerator was similar to the typical contact-mode freestanding triboelectric-layer-based nanogenerators [50]. $V_{\text{max}} = V_{\text{max}}$ because the capacitance between the electrodes was constant [50,51]. According to Eq. (16), the saturation voltage of the capacitor could be charged to 50% of V_{max} , which was consistent with the results observed in this study.

In Niu *et al.*, the charging performance of the nanogenerator with a rectifier was proved to be completely analogous to that of a DC voltage source and its charging behavior depended on the load capacitor [52]. Herein, two capacitors with 10 μF and 1000 μF were separately charged by signal 3 (Figure S7) which had a peak voltage of 8 V, and the charging curves of the two capacitors were compared. The results indicated that the two capacitors finally reached almost the same saturation voltage, and it took longer time for the bigger capacitor to reach the saturation voltage (Figure S8a and Figure S8b). As shown in Table 3, harvesting external energy to charge fibrous air filters and enhance the filtration efficiency is the most common design. In such air filtration systems, an external nanogenerator was employed to harvest energy. The driving mechanism of the nanogenerator included various mechanical movements such as the rotating shaft of a bicycle, human motion, and wind. The external energy to drive this type of self-powered air filter, often exceeded the range that the common ventilation system can provide. For

example, in a self-powered electrostatic air cleaner, the wind used to drive the nanogenerator had the speed of 10.2 to 15.1 m/s [53]. Such a wind speed is far higher than the filtration velocity (2–50 cm/s) in the common ventilation system [54]. By contrast, the SSSAF harvested the innate energy carried by the filtration air flow from the ventilation system without the assistant of external energy harvesting device. Different to the other self-powered air filters, the harvested energy was not applied to charge the filter but employed to inhibit bacteria. Moreover, the filtration efficiency of SSSAF was higher than the most of reported self-powered air filters.

The electrical discharge at a voltage of 4 V, supplied by the SSSAF charged 10 μF capacitors, was applied on the bacteria contaminated surface of the SSSAF for inhibiting the growth of bacteria. Because the 10 μF capacitors could be charged to the saturated voltage of 4 V in ~ 250 s (Fig. 6a), the frequency of the applied electrical discharge was 14 times per hour. As shown in Fig. 6b, the numbers of viable bacteria on both the control sample and test sample decreased over time. When the electrical discharge was applied to *B. subtilis* on the test sample for 5 h, the number of the killed bacteria was 96% of the original bacteria number, and 78% of that on the control sample. The effect of the electrical discharge on the number of viable bacteria was clearly visible in the cultured agar plates (Fig. 6c). Moreover, the electrical discharge was

Table 3

The comparison between SSSAF and other similar self-powered air cleaning devices.

Reference	Fiber type	Particle size	Filtration efficiency	Harvesting energy by filter?	Application of harvested energy	Power source
[53]	–	Flying dust	0.327 g/5h	No	Electrostatic precipitation	Air blower
[55]	Cellulose	2.5 μm	83.78%	No	Filter charging	Bicycle rotating
[15]	Polyimide	33.4 nm	90.60%	No	Filter charging	Motor
[56]	Polyimide	53.3 nm	94.10%	No	Filter charging	Motor
The present study	PVDF	30–500 nm	98%	Yes	Bacteria inhibition	Ventilation system

also effective for inhibiting *E. Coli* which was a Gram-negative bacterium (Figure S9). Similar to the present study, the electrical stimulation was demonstrated to be effective for inhibiting both Gram-positive and Gram-negative bacteria in Daeschlein *et al.*, [57].

Using electric fields for disinfection purposes has been studied for several decades. The method using high voltages of 20 kV/cm or higher has been well known and understood [58,59]. The direct electric current of low amperage has also been proved to effectively inhibit the growth of several bacteria such as *Staphylococcus aureus* and *Proteus mirabilis* [60–62]. The widely acceptable antibacterial mechanism of electrical stimulation is that it disrupts the physiological functions of the microorganisms like the membrane transport [60]. In a recent study, it was revealed that the cell wall is a target in the electrical-inhibition of bacteria [63]. Based on the literature, we believe that the harvested energy of the SSSAF functioned via the discharged current to inhibit the growth of *B. subtilis* and *E. Coli*. In Birbir *et al.*, 100% of extremely halophilic bacteria were killed under the challenge of 0.5 A constant electric current (with 4 V voltage) in 10 min [62]. By contrast, 78% *B. subtilis* bacteria of the control sample were killed in the present study after 70 times of electrical discharge in 5 h. On the one hand, *B. subtilis* is harder to kill because the endospores produced by *B. subtilis* provided additional protection against environmental stresses [64]. On the other hand, the used electric current in the present work was 700nA (with 4 V voltage) and gradually decreased during electrical discharge (Figure S10), which was much lower than that in Birbir *et al.*, [62] and could be responsible for the lower killing rate. However, it should be emphasized that the energy used for bacteria inhibition in this study was supplied by the SSSAF itself; no external power source was needed. Currently, the industrial scale electrospinning equipment is already available. NONWOVENS INDUSTRY announced that its nanofiber pilot equipment can produce the nanofiber membrane with a width of 60 cm and a basic weight of 0.5 g/m² at the production rate of 84 m/min (http://www.nonwovens-industry.com/issues/2017-05/view_features/nanofiber-electrospinning-proves-a-success/). The application of SSSAF in large scale ventilation systems has a bright future.

4. Conclusions

A multifunctional and energy efficient SSSAF was developed to treat multiple contaminants simultaneously. Compared with the smart filters with various commercial sensors, the SSSAF with inherent VOC and pressure drop sensing functions presented the advantages in the product cost and energy consumption. The SSSAF harvested energy from the innate filtration air flow, whereas other nanogenerator based filters relied on external energy input such as the rotating shaft of a bicycle, human motion, and wind. In addition, the harvested energy of SSSAF was applied for bacteria inhibition, which enabled the SSSAF achieving antibacterial property without any additives or external power source.

The average filtration efficiency of the SSSAF for particles in the range of 50–500 nm was 98.51%. The SSSAF achieved the pressure drop sensing function by correlating its pressure drop and piezoelectric signal. Thanks to the swelling property of the PZT/PVDF membrane, the SSSAF showed a sensitive response to ethanol vapor in the concentration range of 50 to 200 ppm. Such polymer based VOC sensors are easy to produce with low cost, and they have great potential in various smart systems. Besides the sensing functions, the SSSAF was used as an energy harvester, and the harvested energy was effectively used to inhibit the growth of bacteria.

Further work is needed to improve the SSSAF. A better structure design would help to enhance the output power of the SSSAF based energy harvester. The VOC sensing property could be improved by employing other polymers or modifying the surface to enhance the affinity between the fibers and VOCs. The sensors based on stimuli-responsive polymers for monitoring wind velocity, temperature and humidity are expected to be integrated into the SSSAF. Our SSSAF is designed to take advantage of the energy carried by the filtration air

flow, which is necessary in any filtration system thus brings a stable and innate energy source. The piezoelectric response and the harvested energy are then used for applications such as assisting sensor functions and bacterial inhibition, thus saving energy and reduce the need for external devices. Overall, this study provides new insight into development of all-in-one smart air filters to handle complex contaminants.

Declaration of Competing Interest

The authors declare that they have no known competing financial interests or personal relationships that could have appeared to influence the work reported in this paper.

Acknowledgements

We thank the support of National Science and Technology Major Project of China (Award ID: 2017YFC0211801; 2016YFC0801704; 2016YFC0203701; 2016YFC0801605; 2019JH2/10100004). The work was partially supported by Center for Filtration Research at University of Minnesota. The authors also thank the financial aid from the project of China Scholarship Council, China.

Appendix A. Supplementary data

Supplementary data to this article can be found online at <https://doi.org/10.1016/j.cej.2021.130247>.

References

- [1] C. Chang, M.E. Gershwin, Indoor air quality and human health, *Clin. Rev. Allergy Immunol.* 27 (2004) 219–239.
- [2] A. Luengas, A. Barona, C. Hort, G. Gallastegui, V. Platel, A. Elias, A review of indoor air treatment technologies, *Rev. Environ. Sci. Bio/Technol.* 14 (3) (2015) 499–522.
- [3] J.D. Spengler, K. Sexton, Indoor air pollution: a public health perspective, *Science* 221 (1983) 9–17.
- [4] A.A. Haleem Khan, S. Mohan Karuppaiyl, Fungal pollution of indoor environments and its management, *Saudi J. Biol. Sci.* 19 (4) (2012) 405–426.
- [5] S.C. Sofuoğlu, G. Aslan, F. Inal, A. Sofuoğlu, An assessment of indoor air concentrations and health risks of volatile organic compounds in three primary schools, *Int. J. Hyg. Environ. Health* 214 (1) (2011) 36–46.
- [6] K.-H. Kim, E. Kabir, S.A. Jahan, Airborne bioaerosols and their impact on human health, *J. Environ. Sci.* 67 (2018) 23–35.
- [7] H.-J. Kim, S.J. Park, C.S. Park, T.-H. Lee, S. Hun Lee, T.H. Ha, H.-i. Kim, J. Kim, C.-S. Lee, H. Yoon, O.S. Kwon, Surface-modified polymer nanofiber membrane for high-efficiency microdust capturing, *Chem. Eng. J.* 339 (2018) 204–213.
- [8] N.A. McLarnon, G. Edwards, J.G. Burrow, W. Maclaren, K.E. Aidoo, M. Hefher, The efficiency of an air filtration system in the hospital ward, *Int. J. Environ. Health Res.* 16 (4) (2006) 313–317.
- [9] W. He, Y. Guo, R. Shen, Q. Liu, J. Liu, Enhancement of filtration performance of polyester (PET) filters by compositing with schorl powder, *Powder Technol.* 342 (2019) 321–327.
- [10] C.N. Davies, *Air Filtration*, Academic Press, London, 1976.
- [11] W.C. Hinds, *Aerosol Technology*, John Wiley & Sons, New York, 1982.
- [12] R.C. Brown, *Air Filtration*, Pergamon Press, Oxford, 1988.
- [13] N. Nassif, The impact of air filter pressure drop on the performance of typical air-conditioning systems, *Build. Simul.* 5 (4) (2012) 345–350.
- [14] C.B. Han, T. Jiang, C. Zhang, X. Li, C. Zhang, X. Cao, Z.L. Wang, Removal of particulate matter emissions from a vehicle using a self-powered triboelectric filter, *ACS nano* 9 (12) (2015) 12552–12561.
- [15] G.Q. Gu, C.B. Han, C.X. Lu, C. He, T. Jiang, Z.L. Gao, C.J. Li, Z.L. Wang, Triboelectric nanogenerator enhanced nanofiber air filters for efficient particulate matter removal, *ACS nano* 11 (6) (2017) 6211–6217.
- [16] C.X. Li, S.Y. Kuang, Y.H. Chen, Z.L. Wang, C. Li, G. Zhu, In situ active poling of nanofiber networks for gigantically enhanced particulate filtration, *ACS Appl. Mater. Interfaces* 10 (29) (2018) 24332–24338.
- [17] Y. Zhao, Z.X. Low, S. Feng, Z. Zhong, Y. Wang, Z. Yao, Multifunctional hybrid porous filters with hierarchical structures for simultaneous removal of indoor VOCs, dusts and microorganisms, *Nanoscale* 9 (2017) 5433.
- [18] Y. Zeng, R. Xie, J. Cao, Z. Chen, Q. Fan, B. Liu, X. Lian, H. Huang, Simultaneous removal of multiple indoor-air pollutants using a combined process of electrostatic precipitation and catalytic decomposition, *Chem. Eng. J.* 388 (2020), 124219.
- [19] R. Maus, A. Goppelsröder, H. Umhauer, Survival of bacterial and mold spores in air filter media, *Atmos. Environ.* 35 (1) (2001) 105–113.
- [20] J.D. Miller, D.R. McMullin, Fungal secondary metabolites as harmful indoor air contaminants: 10 years on, *Appl. Microbiol. Biotechnol.* 98 (2014) 9953–9966.

- [21] Z. Wang, Z. Pan, J. Wang, R. Zhao, A novel hierarchical structured poly(lactic acid)/titania fibrous membrane with excellent antibacterial activity and air filtration performance, *J. Nanomater.* 2016 (2016) 1–17, <https://doi.org/10.1155/2016/6272983>.
- [22] A. Cooper, R. Oldinski, H. Ma, J.D. Bryers, M. Zhang, Chitosan-based nanofibrous membranes for antibacterial filter applications, *Carbohydr. Polym.* 92 (1) (2013) 254–259.
- [23] Y.-S. Ko, Y.H. Joe, M. Seo, K. Lim, J. Hwang, K. Woo, Prompt and synergistic antibacterial activity of silver nanoparticle-decorated silica hybrid particles on air filtration, *J. Mater. Chem. B* 2 (39) (2014) 6714–6722.
- [24] Z. Zhong, Z. Xu, T. Sheng, J. Yao, W. Xing, Y. Wang, Unusual air filters with ultrahigh efficiency and antibacterial functionality enabled by ZnO nanorods, *ACS Appl. Mater. Interfaces* 7 (38) (2015) 21538–21544.
- [25] Z. Sun, Y. Yue, W. He, F. Jiang, C.-H. Lin, D.Y.H. Pui, Y. Liang, J. Wang, The antibacterial performance of positively charged and chitosan dipped air filter media, *Build. Sci.* 180 (2020) 107020, <https://doi.org/10.1016/j.buildenv.2020.107020>.
- [26] S. Kumar, A.G. Fedorov, J.L. Gole, Photodegradation of ethylene using visible light responsive surfaces prepared from titania nanoparticle slurries, *Appl. Catal. B* 57 (2) (2005) 93–107.
- [27] K. Everaert, J. Baeyens, Catalytic combustion of volatile organic compounds, *J. Hazard. Mater.* 109 (2004) 113–139.
- [28] L. Lin, Y. Chai, B. Zhao, W. Wei, D. He, B. He, Q. Tang, Photocatalytic oxidation of organics in water using pure and silver-modified titanium dioxide particles, *Open J. Inorg. Chem.* (2013), <https://doi.org/10.4236/ojic.2013.31003>.
- [29] J.-J. Li, Y.-N. Zhou, Z.-H. Luo, Smart fiber membrane for pH-induced oil/water separation, *ACS appl. Mater. Interfaces* 7 (35) (2015) 19643–19650.
- [30] S.W. Hong, D.Y. Kim, J.U. Lee, W.H. Jo, Synthesis of polymeric temperature sensor based on photophysical property of fullerene and thermal sensitivity of Poly(N-isopropylacrylamide), *Macromolecules* 42 (7) (2009) 2756–2761.
- [31] A.V. Shirinov, W.K. Schomburg, Pressure sensor from a PVDF film, *Sensor. Actuat. A-Phys.* 142 (1) (2008) 48–55.
- [32] D. Rana, K. Bag, S.N. Bhattacharyya, B.M. Mandal, Miscibility of poly(styrene-co-butyl acrylate) with poly(ethyl methacrylate): existence of both UCST and LCST, *J. Polym. Sci., Part B: Polym. Phys.* 38 (3) (2000) 369–375.
- [33] D. Rana, B.M. Mandal, S.N. Bhattacharyya, Miscibility and phase diagrams of poly(phenyl acrylate) and poly(styrene-co-acrylonitrile) blends, *Polymer* 34 (7) (1993) 1454–1459.
- [34] D. Rana, B.M. Mandal, S.N. Bhattacharyya, Analogue calorimetry of polymer blends: poly(styrene-co-acrylonitrile) and poly(phenyl acrylate) or poly(vinyl benzoate), *Polymer* 37 (1996) 2439–2443.
- [35] B.C. Chakraborty, D. Ratna, in: *Polymers for Vibration Damping Applications*, Elsevier, 2020, pp. 143–201, <https://doi.org/10.1016/B978-0-12-819252-8.00004-5>.
- [36] A.K. Zak, W.C. Gan, W.H.A. Majid, M. Darroudi, T.S. Velayutham, Experimental and theoretical dielectric studies of PVDF/PZT nanocomposite thin films, *Ceram. Int.* 37 (5) (2011) 1653–1660.
- [37] T. Greeshma, R. Balaji, S. Jayakumar, PVDF phase formation and its influence on electrical and structural properties of PZT-PVDF composites, *Ferroelectr. Lett. Sect.* 40 (1–3) (2013) 41–55.
- [38] H. Shao, J. Fang, H. Wang, T. Lin, Effect of electrospinning parameters and polymer concentrations on mechanical-to-electrical energy conversion of randomly-oriented electrospun poly(vinylidene fluoride) nanofiber mats, *RSC Adv.* 5 (19) (2015) 14345–14350.
- [39] W.-F. Leung, C.-H. Hung, P.-T. Yuen, Effect of face velocity, nanofiber packing density and thickness on filtration performance of filters with nanofibers coated on a substrate, *Sep. Purif. Technol.* 71 (1) (2010) 30–37.
- [40] S.-H. Huang, C.-W. Chen, Y.-M. Kuo, C.-Y. Lai, R. McKay, C.-C. Chen, Factors affecting filter penetration and quality factor of particulate respirators, *Aerosol Air Qual. Res.* 13 (1) (2013) 162–171.
- [41] D.Q. Chang, S.C. Chen, A.R. Fox, A.S. Viner, D.Y. Pui, Penetration of sub-50 nm nanoparticles through electret HVAC filters used in residence, *Aerosol Sci. Technol.* 49 (2015) 966–976.
- [42] Z. Pi, J. Zhang, C. Wen, Z.-B. Zhang, D. Wu, Flexible piezoelectric nanogenerator made of poly(vinylidene fluoride-co-trifluoroethylene)(PVDF-TrFE) thin film, *Nano Energy* 7 (2014) 33–41.
- [43] R.K. Mobley, *Plant Engineer's Handbook: Vibration fundamentals*, Elsevier (2001) 723–755.
- [44] S.C. Kim, J. Wang, W.G. Shin, J.H. Scheckman, D.Y. Pui, Structural properties and filter loading characteristics of soot agglomerates, *Aerosol Sci. Technol.* 43 (2009) 1033–1041.
- [45] E.K. Tan, G. Rughoobur, J. Rubio-Lara, N. Tiwale, Z. Xiao, C.A. Davidson, L. G. Ochipinti, Nanofabrication of conductive metallic structures on elastomeric materials, *Sci. Rep.* 8 (2018) 1–9.
- [46] P. Sachinidou, C. Heuschling, J. Schaniel, J. Wang, Investigation of surface potential discharge mechanism and kinetics in dielectrics exposed to different organic solvents, *Polymer* 145 (2018) 447–453.
- [47] S. Benltoufa, F. Fayala, S.B. Nasrallah, Determination of yarn and fiber diameters after swelling using a capillary rise method, *J. Text. Inst.* 103 (2012) 517–522.
- [48] Y. Zi, J. Wang, S. Wang, S. Li, Z. Wen, H. Guo, Z.L. Wang, Effective energy storage from a triboelectric nanogenerator, *Nat. Commun.* 7 (2016) 1–8.
- [49] H. Wang, H.W. Lee, Y. Deng, Z. Lu, P.C. Hsu, Y. Liu, D. Lin, Y. Cui, Bifunctional non-noble metal oxide nanoparticle electrocatalysts through lithium-induced conversion for overall water splitting, *Nat. Commun.* 6 (2015) 1–8.
- [50] S. Niu, Y. Liu, X. Chen, S. Wang, Y.S. Zhou, L. Lin, Y. Xie, Z.L. Wang, Theory of freestanding triboelectric-layer-based nanogenerators, *Nano Energy* 12 (2015) 760–774.
- [51] S. Wang, Y. Xie, S. Niu, L. Lin, Z.L. Wang, Freestanding triboelectric-layer-based nanogenerators for harvesting energy from a moving object or human motion in contact and non-contact modes, *Adv. Mater.* 26 (18) (2014) 2818–2824.
- [52] S. Niu, Y. Liu, Y.S. Zhou, S. Wang, L. Lin, Z.L. Wang, Optimization of triboelectric nanogenerator charging systems for efficient energy harvesting and storage, *IEEE Trans. Electron Devices* 62 (2014) 641–647.
- [53] S. Chen, C. Gao, W. Tang, H. Zhu, Y. Han, Q. Jiang, T. Li, X. Cao, Z. Wang, Self-powered cleaning of air pollution by wind driven triboelectric nanogenerator, *Nano Energy* 14 (2015) 217–225.
- [54] J. Wang, P. Tronville, Toward standardized test methods to determine the effectiveness of filtration media against airborne nanoparticles, *J. Nanopart. Res.* 16 (2014) 1–33.
- [55] J. Mo, C. Zhang, Y. Lu, Y. Liu, N. Zhang, S. Wang, S. Nie, Radial piston triboelectric nanogenerator-enhanced cellulose fiber air filter for self-powered particulate matter removal, *Nano Energy* 78 (2020), 105357.
- [56] G.Q. Gu, C.B. Han, J.J. Tian, T. Jiang, C. He, C.X. Lu, Y. Bai, J.H. Nie, Z.L. Wang, Triboelectric nanogenerator enhanced multilayered antibacterial nanofiber air filters for efficient removal of ultrafine particulate matter, *Nano Res.* 11 (2018) 4090–4101.
- [57] G. Daeschlein, O. Assadian, L.C. Kloth, C. Meinel, F. Ney, A. Kramer, Antibacterial activity of positive and negative polarity low-voltage pulsed current (LVPC) on six typical Gram-positive and Gram-negative bacterial pathogens of chronic wounds, *Wound Repair Regen.* 15 (3) (2007) 399–403.
- [58] A. Mizuno, Y. Hori, Destruction of living cells by pulsed high-voltage application, *IEEE Trans. Ind. Appl.* 24 (3) (1988) 387–394.
- [59] A. SALE, W. HAMILTON, Effects of high electric fields on microorganisms: I. Killing of bacteria and yeasts, *Biochim. Biophys. Acta, Gen. Subj.* 148 (3) (1967) 781–788.
- [60] W.-K. Liu, S.E. Tebbs, P.O. Byrne, T.S.J. Elliott, The effects of electric current on bacteria colonising intravenous catheters, *J. Infect.* 27 (3) (1993) 261–269.
- [61] X.G. Li, H.B. Cao, J.C. Wu, K.T. Yu, Inhibition of the metabolism of nitrifying bacteria by direct electric current, *Biotechnol. Lett.* 23 (2001) 705–709.
- [62] Y. Birbir, M. Birbir, Inactivation of extremely halophilic hide-damaging bacteria via low-level direct electric current, *J. Electrostat.* 64 (12) (2006) 791–795.
- [63] F. Pillet, C. Formosa-Dague, H. Baaziz, E. Dague, M.P. Rols, Cell wall as a target for bacteria inactivation by pulsed electric fields, *Sci. Rep.* 6 (2016) 1–8.
- [64] A. Mai-Prochnow, M. Clauson, J. Hong, A.B. Murphy, Gram positive and Gram negative bacteria differ in their sensitivity to cold plasma, *Sci. Rep.* 6 (2016) 38610.